# THE LONG AND WINDING ROAD THAT LEADS TO HOMOGENISATION OF KRESLING ORIGAMI

EMILIO TURCO\*, EMILIO BARCHIESI\*, AND FRANCESCO DELL'ISOLA°

ABSTRACT. What are the geometrical and mechanical properties ruling bistability of Kresling origami metamaterials? How can we tune the magnitude of their axial-torsional coupling? Complete answers to these compelling questions cannot be found in the scientific literature, as the intertwining between bistability, axial-torsional coupling and an other significant behaviour, namely transverse dilation/contraction, remains mostly uninvestigated. This contribution aims at shedding light on this intertwining, through the use of a discrete model of Kresling origami that takes into account folding resistance. The present study is mostly computational and involves both pre- and post-critical analyses. It is based on displacement controlled tests – shearing and axial shortening/lengthening. Single-storey Kresling origami's are first considered, preliminarly to multiple-storey tubes, where buckling is observed. Several parameters are taken into account such as the number of storeys, stretching and folding stiffnesses, and – for shearing tests – the prescribed displacement direction in the transversal plane. The ultimate goal of the paper is to provide evidence that can be useful in the construction of homogenised continuum models of Kresling origami metamaterials.

#### 1. Introduction

Research on metamaterials is one of the most interesting field in today's applied science. This is testified by the high amount of papers on the topic. The term metamaterial, which comes from the Greek word  $\mu\varepsilon\tau\alpha$  (meta), meaning "beyond" or "after", and the Latin word materia, meaning "matter" or "material", stands for any material with an architecture that has been engineered to achieve a property that is rarely observed in naturally occurring materials.

Generally, metamaterials are made up of assemblies of several elements like rods, beams, plates and solids, each realised by using, possibly, different base materials. These assemblies, whose size is smaller than the wavelengths of the phenomena they are aimed at affecting, constitute the so-called unit cell, which is repeated in one, two or three directions. The properties of metamaterials derive from the arrangement of their elements or unit cells rather than from their base materials. Therefore, shape, dimension, orientation, and arrangement are the basic ingredients the exotic properties of metamaterial are due. The study of material architectures that confer the desired behaviour is clearly a topic of great interest in several scientific and engineering disciplines, as the desired behaviour could involve acoustics, electric, magnetics, mechanical, and/or thermal phenomena, only to name a few.

A solid theoretical ground is necessary to design or study metamaterial architectures, as their complexity and huge variety often pose an insurmountable challenge to empirical investigation. When theoretical models, be them continuous or discrete, cannot be used to get predictions without the need for applying numerical approximation algorithms, so-called numerical experiments are performed. These experiments, provided that the underlying theoretical model is predictive, *i.e.*, it gives reliable predictions, are essentially inexpensive and allow for bypassing all the difficulties that are usually encountered when real experiments are performed. At these conditions, it is clear why a huge quantity of numerical experiments can be performed to understand the behaviours conferred by a given material architecture. These advantages comes at the only price of choosing appropriate numerical data, usually appearing in a constitutive law. Speaking about mechanical metamaterials, as an instance, the characterisation of the in-plane bending of a constituting beam described through the Euler–Bernoulli model requires the specification of a parameter related to its base material, such as its Young modulus, and a parameter related to the

Date: March 21, 2024.

Key words and phrases. Kresling origami, mechanical metamaterials, nonlinear analysis, buckling, bistability. Preprint submitted to International Journal of Non-Linear Mechanics.

<sup>&</sup>lt;sup>1</sup>A quick search of the word metamaterial on Google at the beginning of 2024 gives more than six millions of results.

geometry of its cross section, such as its quadratic inertia moment with respect to the line orthogonal to the bending plane.

Theoretical modelling hence plays a key role in metamaterials design. With reference to mechanical metamaterials, it is noteworthy to mention that simple yet effective models for beam [1, 2, 3] elements, grain assemblies [4, 5, 6], and more complex structures [7, 8] have been recently proposed in the literature along the lines of the model used in this paper to describe Kresling origami metamaterials. Coming to the topic dealt with in the present contribution, Kresling origami tube metamaterials (in short K-tubes) have attracted the interest of many researchers in the last years. Figure 1 shows several examples of single-storey  $^2$  K-tubes, each having a polygonal base with a different number of sides: 3, 4, 5, 6, 8 and 12.

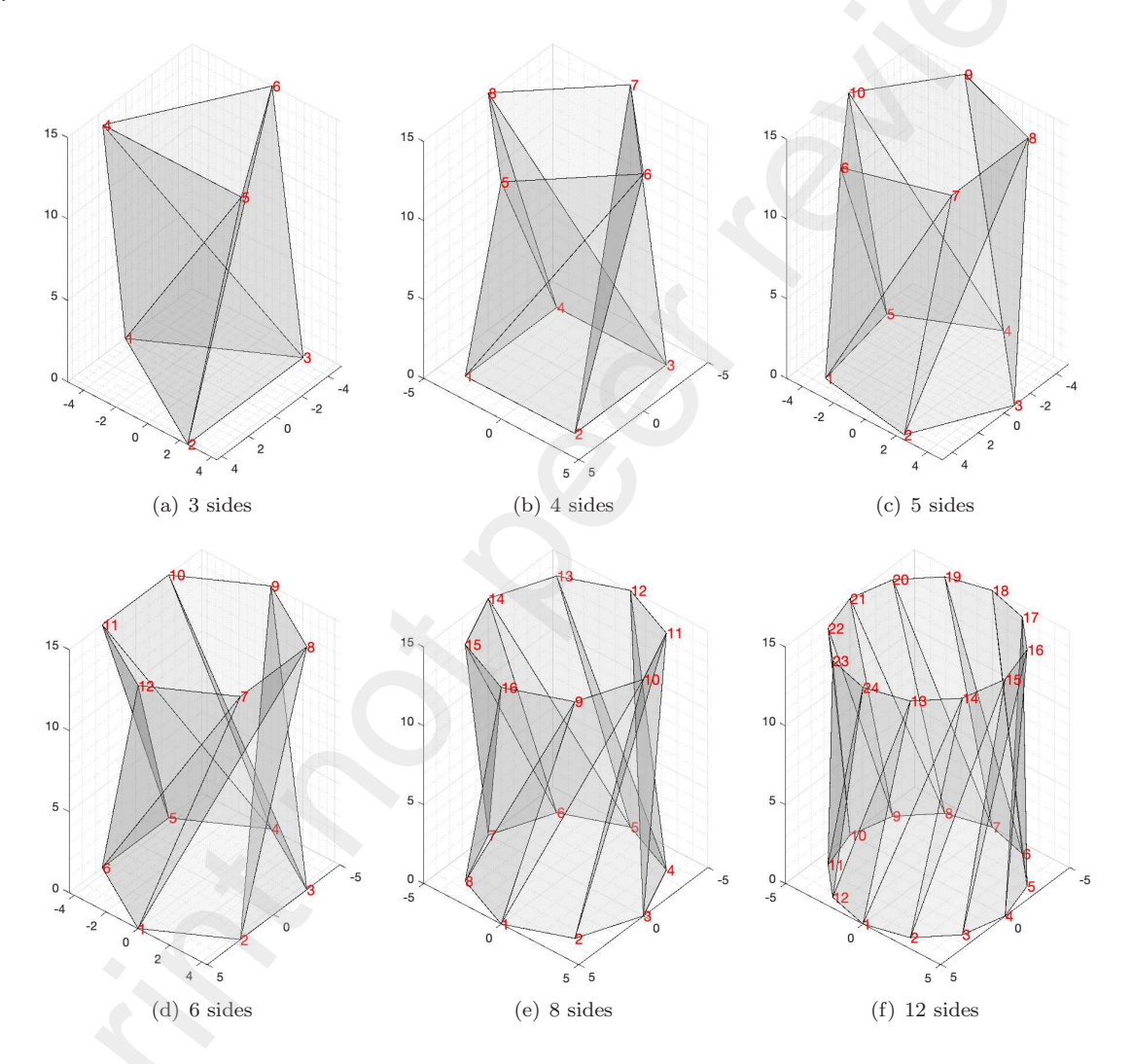


FIGURE 1. Single-stage K-tubes based on regular polygons with 3, 4, 5, 6, 8 and 12 sides.

These structures exhibit several interesting mechanical features. One of them is described in [9] by means of some numerical simulations based on a discrete mechanical model taking into account: i) the in-plane affine deformation of the facets of the K-tube; ii) the folding of two adjacent facets around their shared side, i.e., the associated crease. Detailed presentations of modelling approaches based on these assumptions are reported in the papers [10, 11]. While being the approaches presented in the two last papers slightly different, they essentially make use of the same strain energy and come up with the same governing equations. The main difference between these two approaches resides in the fact that

<sup>&</sup>lt;sup>2</sup>Henceforth the term *stage* will be used interchangeably with the term *storey*.

[11] considers the contribution of the kinetic energy as non-negligible with respect to the strain energy. Therefore, it can handle full dynamic problems.

The complexity of the mechanical behaviours of K-tubes, in addition to being interesting *per se*, can be exploited to realise several technological devices that can be synthetically grouped as follows:

- (1) mechanical pixels, see [12], by harnessing their chirality and the consequent coupling between lengthening/shortening and twisting;
- (2) robotic locomotion systems capable to swim in fluids [13];
- (3) soft robotic arms [14, 15];

50

55

- (4) inflatable/collapsible tubes [16], including devices that can be used in several medical applications such as stent grafts [17];
- (5) mechanical logical ports, as shown in [18];
- (6) devices that work as force reducers [19] or stiffeners [20];
- (7) biomimetic metamaterials characterised by phase transformation [21] and haptic capabilities [22];
- (8) deployable structures, see [23, 24, 25], including antennas and other devices for space missions, see [26].

While K-tubes are well known for the fact that their geometry induces the coupling of axial short-ening/lengthening and the rotation of the polygonal cross-section, see Fig. 1, along with the fact that they can show a bistable behaviour in lengthening/shortening, they have been mostly studied without taking into account resistance to foldability, which determines in lengthening/shortening tests a dilation/contraction of the polygonal cross-section.<sup>3</sup> The intertwining between bistability, axial-torsional coupling and transverse dilation/contraction remains mostly uninvestigated.

This work reports on some numerical experiments finalised to the understanding of the mechanical behaviour of K-tubes, forming the ground for constructing -e.g., by homogenisation - continuum models of K-tubes by following the guidelines reported in [27, 28, 29]. We firstly determine and select in Sec. 2 the geometrical necessary conditions to have bistability, namely those properties such that there exists a configuration different from the initial one such that all creases remain undeformed. The description of the employed discrete model, along with a brief description of the numerical methodology employed to compute the dynamic evolution of the studied system, is reported in Sec. 3. Several numerical simulations are reported and thoroughly discussed in Sec. 4, aiming at highlighting the main properties of the mechanical behaviour of K-tubes. The analysis begins from single-stage tubes, *i.e.*, the elementary unit cell, and gets to twenty-stage tubes passing trough four-stage tubes. The analysis is particularly concerned with sensitivity to: i) number of stages; ii) stiffness parameters; iii) load typology and, for shearing tests, iv) direction of transverse prescribed displacement. Finally, concluding remarks anticipate future challenges related to the presented research in Sec. 5.

### 2. Relationship between geometry and bistability of K-tubes

It is well-known that Kresling origami metamaterials with null resistance to folding can exhibit bistability, namely there might exist a configuration that, as the initial one, corresponds to a null deformation energy and cannot be obtained by rigid transformation of the initial one. In other words, the strain energy associated to a one-stage Kresling tube as a function of its current height in a lengthening/shortening test might exhibit a double-well shape, analogously to the Von Mises arch. This property is mentioned and studied by several papers in the literature, like, e.g., [30]. In what follows, we elaborate more on this property, using a simple geometrical argument to determine whether the above-mentioned double well can exist and where it is located. Numerical simulations will then be employed to verify the actual achievement of bistability for geometrical parameters fulfilling the found conditions and null folding resistance. Further simulations considering the same geometrical parameters but non-null folding resistance will show that folding stiffness increases the total energy level for each eight and, therefore, also that of a well. For the folding stiffness above a certain threshold value, the strain energy as a function of the eight does not exhibit anymore a double-well shape.

<sup>&</sup>lt;sup>3</sup>We find especially interesting – although this has not been either formalised or proved – the similarity of the deformation of a K-tube when shortening or lengthening and the propagation of longitudinal waves fulfilling the sine-Gordon equation.

Let us consider a K-tube characterised by a regular polygonal cross-section with N sides inscribed in a circle of radius R. Let the length of the sides of the polygonal cross-section be denoted with the symbol  $\ell$  and the eight of the tube with h, see Fig. 2.

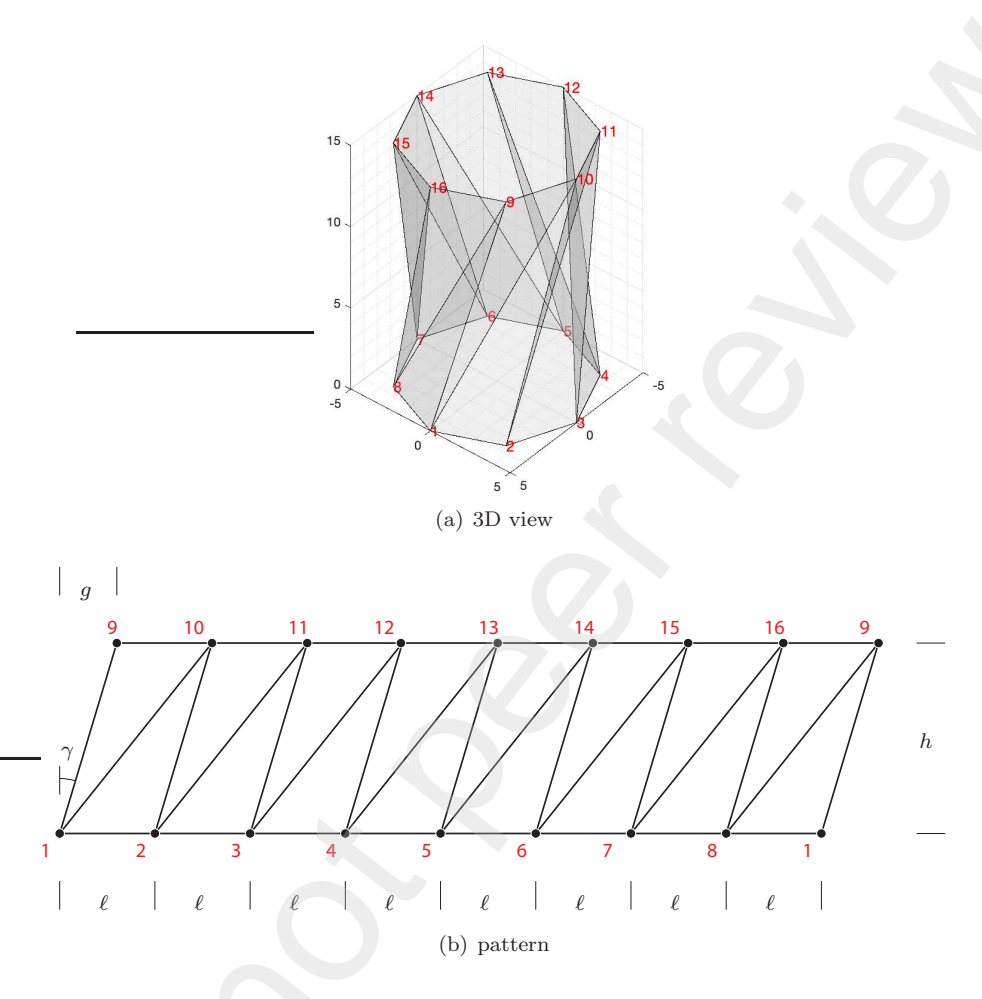


FIGURE 2. Single-stage K-tube whose cross-section is a regular octagon: 3D view of the structure with node numbering (a) and its planar pattern (b).

Looking at one of the triangles which form the K-tube – say that having as vertices the nodes i, j and k – it is straightforward to see that there could exist a different, congruent, triangle, with a common side, such that its vertices lie on the cylindrical surface depicted in violet in Fig. 3. Such a triangle is depicted in red in Fig. 3 and is obtained by a rotation around the horizontal side of the first one, *i.e.*, that lying on a plane identified by a polygonal cross-section, in-between node i and j. The in-plane deformation energy stored to this triangular facet is null, since each side does not experience any stretch. This argument can be applied to all the facets of the tube at once, taking into account kinematic compatibility, *i.e.*, that facets have common sides. Therefore, if any such un-stretched non-initial configuration exists for a facet, then it exists for all the facets and there hence exists a deformed configuration of the tube such that each facet has not undergone any in-plane deformation. To seek analytically the red triangle, one should compute the intersection among the cylinder in violet and the circle lying on the plane p – whose unit normal vector  $\mathbf{n}$  lies on i-j side and contains the point o – having the point o has its centre and r as radius, see again Fig. 3. This circle is obtained as the intersection of the sphere s of radius s, equal to the distance in-between s and s (depicted in dashed green), centred in s.

In the orthogonal reference frame depicted in Fig. 3, the two positions (denoted with the indices k and h) i.e., initial and non-initial, corresponding to zero in-plane strain energy can be analytically computed

This preprint research paper has not been peer reviewed. Electronic copy available at: https://ssrn.com/abstract=4783149

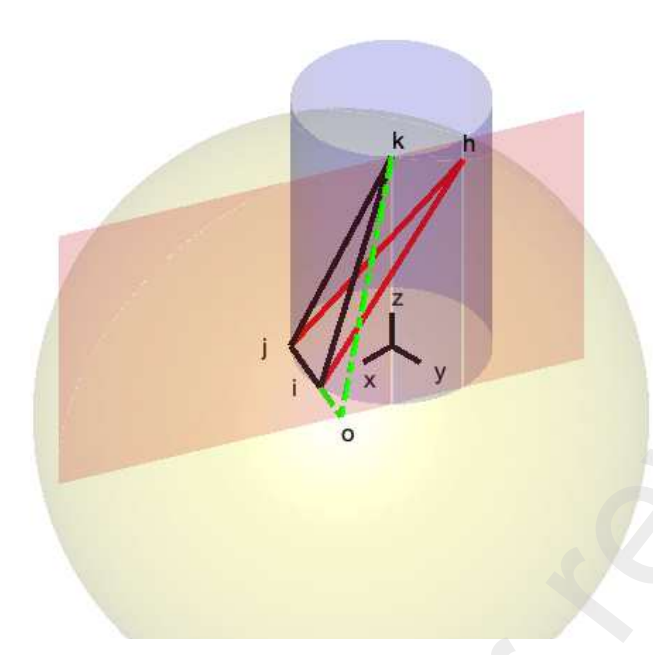


FIGURE 3. Geometrical illustration of Kresling tube bistability.

from the following system

115

120

130

$$\begin{cases} x^{2} + y^{2} = R^{2}, & \text{equation of the cylinder } c \text{ having radius } R, \\ 0 \leq z \leq h, & \text{bounds on the height } h \text{ of the cylinder}, \\ (\mathbf{x} - \mathbf{x}_{o}) \cdot (\mathbf{x} - \mathbf{x}_{o}) = r^{2}, & \text{equation of the sphere } s \text{ centered in } o \text{ having radius } r, \\ \mathbf{n} \cdot (\mathbf{x} - \mathbf{x}_{o}) = 0, & \text{equation of the plane } p, \end{cases}$$

$$(1)$$

where the position vector  $\mathbf{x}_o$  of the point o and the unit vector  $\mathbf{n}$  are expressed in terms of the position vectors of the triangle vertices i, j and k by the following formulas

$$\mathbf{x}_{o} = \mathbf{x}_{j} + \frac{(\mathbf{x}_{k} - \mathbf{x}_{i}) \cdot (\mathbf{x}_{i} - \mathbf{x}_{j})}{\|(\mathbf{x}_{i} - \mathbf{x}_{j})\|^{2}} (\mathbf{x}_{i} - \mathbf{x}_{j}),$$

$$\mathbf{n} = \frac{(\mathbf{x}_{i} - \mathbf{x}_{j})}{\|\mathbf{x}_{i} - \mathbf{x}_{j}\|}.$$
(2)

The solution of this system admits the following cases:

- (1) there is only one solution, *i.e.* the plane containing the circle is tangent to the cylinder, therefore only the reference solution is a zero-energy state when no folding energy is considered and bistability does not occur;
- (2) there are two solutions, *i.e.* besides the reference state there exists an additional zero-energy state when no folding energy is considered.

Clearly, these cases depend upon the geometry of the considered tube. Therefore, the discussion above implies that bistability occurs only in a sub-class of K-tubes, which can be defined in terms of tube height H, side length  $\ell$  and gap g, see Fig. 2. As an instance, for a K-tube based on a regular octagon, N=8, inscribed in a circle of radius R=5 having height H=5 and with a relative rotation between the two octagons  $\vartheta_0=45^\circ$ , therefore  $g=\ell$ , it is simple to verify that bistability occurs for  $h/\ell>1.55$ . This opens the way towards selecting those K-tubes admitting bistability. For special values of  $g/\ell$  and  $h/\ell$ , namely  $g/\ell=1$  and  $h/\ell=3.92$ , using the model that will be introduced in the next section, a numerical simulation is performed for a single-stage tube in an axial shortening test, neglecting the strain energy associated to folding around creases. The tube only shortens axially, and its cross-section rotates and dilates/contracts homothetically. Figure 4 shows the time evolution of the displacement coordinates of

<sup>&</sup>lt;sup>4</sup>All the quantities reported in this work are expressed in MKS system of units, angles are measured in degree.

one of the nodes at the top base of the tube (a), of the energies – kinetic, stretching, and folding – of the whole K-tube (b) and the stretching energy of the sides 1-9 (c), 8-9 (d), and 9-10 (e). Bistability is indeed observed.

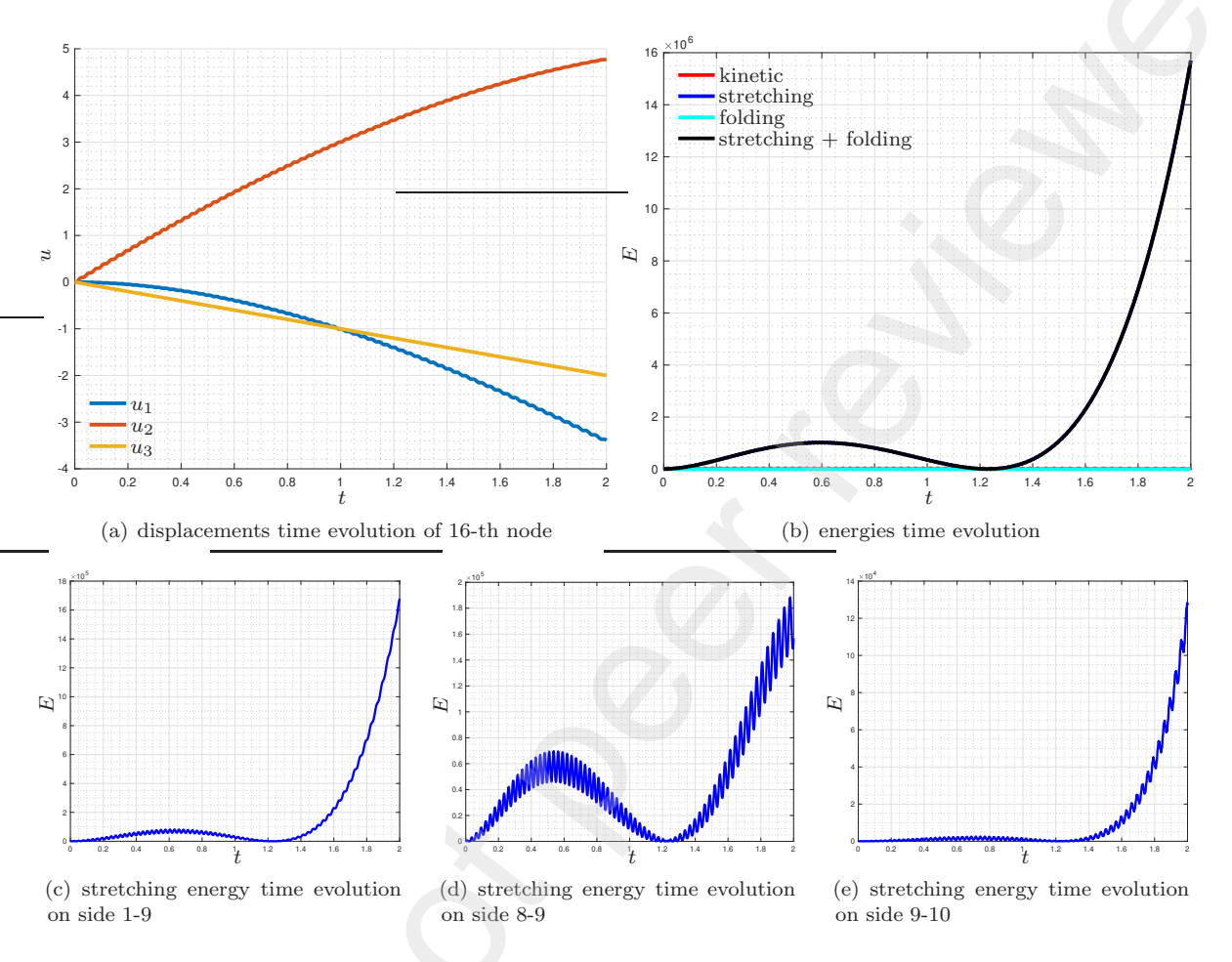


FIGURE 4. Single-stage K-tube subjected to a shortening test: time evolution of the coordinates of the displacement of the 16-th node (a), time evolution of energies for the whole K-tube (b), and stretching energy evolution for the sides 1-9 (c), 8-9 (d), and 9-10 (e).

Let us now focus on the influence of the folding resistance on bistability. Figure 5 reports, besides kinetic energy – which is negligible – in red color, the stretching and folding energies for the whole K-tube, in blue and cyan colors respectively, along with their sum, in black, for the ratio a/b equal to  $10^5.5$  Looking at the curve corresponding to the sum of stretching and folding energies for the whole K-tube, we observe again a double-well, but the presence of folding energy somewhat hinders the second well, which is due to the fact that stretching energy vanishes. Obviously, for values of the ratio a/b lower than  $10^5$ , *i.e.*, increasing b for a fixed, the effect due to the folding energy prevails over that due to the stretching energy, producing as a result that the second well is faint and, eventually, missing.

The plot in Fig. 6 reports, for b = 0, on the left vertical axis, the normalised rotation (normalisation is performed with respect to the angle  $\vartheta_0$  representing the angle between two adjacent polygonal cross-sections in the initial configuration) of the polygonal cross section and, on the right vertical axis, the relative radius change in the tube radius, namely its *stenosis*, against the normalised relative tube height

 $<sup>^{5}</sup>$ The meaning of the stiffness parameters a and b will be better defined below. Here, it is enough to know that a is the stiffness parameter which rules the stretching of each facet, while b is the stiffness parameter which rules the folding of two facets sharing a side.

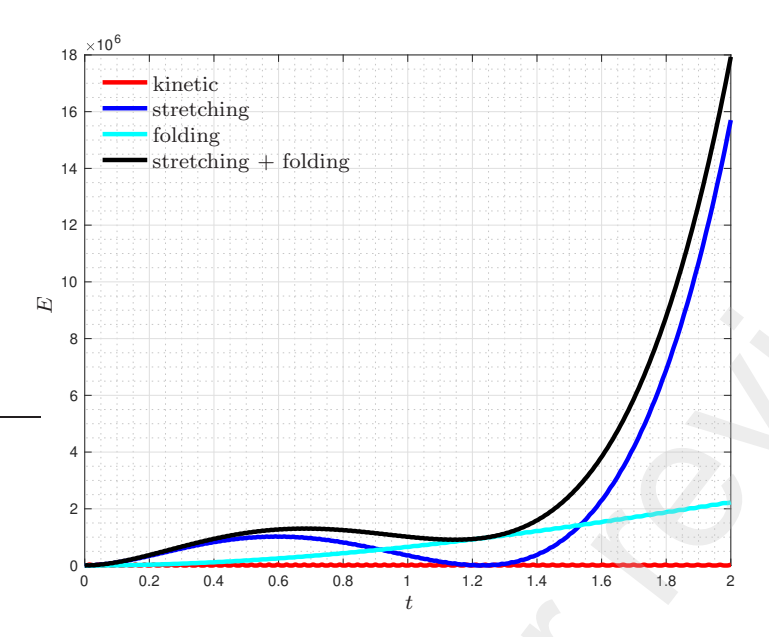


FIGURE 5. Single-stage K-tube subjected to a shortening test: influence of folding resistance on tube bistability for  $a/b = 10^5$ .

change. It is seen that the rotation of the top surface of the tube achieves approximately 71° while the tube stenosis reaches approximatively the value of 1.8, corresponding to a homothetic deformation of the octagonal cross-section where each side has an elongation equal to 36%. We observe that the curve representing the extent of the dilation/contraction of the polygonal cross-section is practically linear, whereas that for the rotation exhibits a non-monotonous behaviour before assuming a monotonous superlinear one.

150

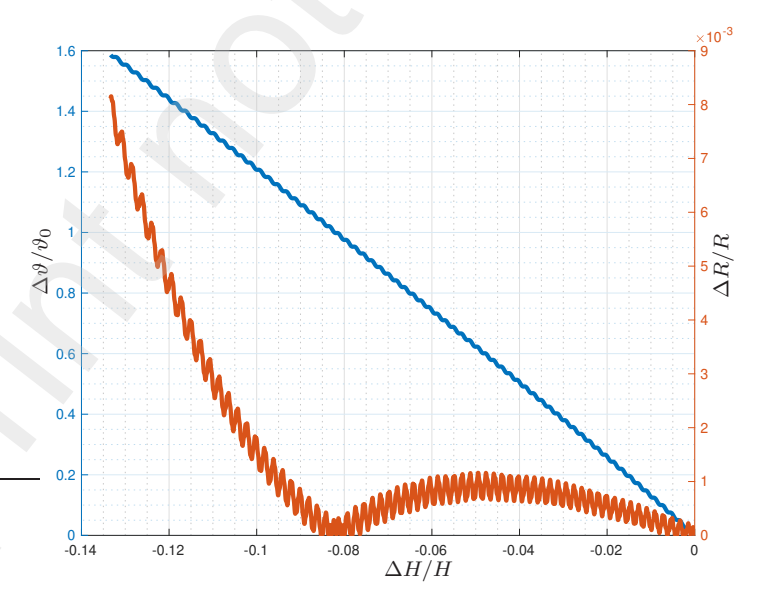


FIGURE 6. Single-stage K-tube subjected to a shortening test: normalised rotation  $\Delta \vartheta/\vartheta_0$  – in blue – and normalised stenosis  $\Delta R/R$  – in red – versus normalised shortening  $\Delta H/H$  for b=0.

Figure 7(a) reports, for b=0, the time evolution of the eight top nodes' vertical reactions. It is possible to detect, besides the point corresponding to the initial configuration, a point where the vertical components of the top-node reactions are zero, which is in agreement with the bistability feature. Figure 7(b) reports, again for b=0, the norm of the vector collecting all the vertical reactions against the norm of the vector collecting the nodal displacements. It is possible to detect, besides the point corresponding to the initial undeformed configuration, a point where all reactions are zero, which is a further confirmation of the bistability feature. It has also to be noted that a sharp increase of the reaction vector norm immediately after the second zero-energy state is observed.

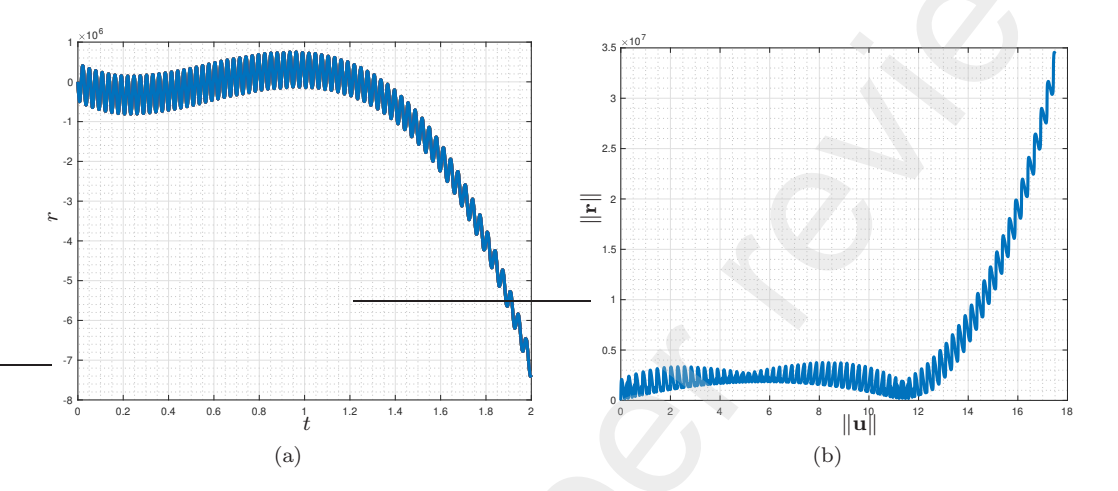


FIGURE 7. Single-stage K-tube subjected to a shortening test: time evolution of the top nodes vertical reaction r (a) and reaction vector norm  $\|\mathbf{r}\|$  vs. displacement vector norm  $\|\mathbf{u}\|$  (b).

## 3. Numerical computation of Kresling tube metamaterials dynamics

Kresling tubes are geometrically specified in terms of some parameters such as the number of nodes N lying on a level and the quantities  $\ell$ , H, and g in Fig. 2, which reports both the three-dimensional view of the K-tube and its planar pattern. Such parameters, along with those defining mechanically the material the tube is constituted of, such as the mass density, the Young's modulus and the Poisson's ratio allow to build a model aimed at describing the evolution of the Kresling tube when subjected to boundary conditions and external loads or given displacements.

In the scientific literature there exist several contributions reporting numerical simulations of metamaterials possessing an origami-patterned microstructure, such as Miura, Kresling, egg-box, etc. Among all these contributions, it is worth to mention here [31, 32], which does not take into account the in-plane deformability of facets, and [10] which, conversely, takes it into account by substituting the facet with an equivalent truss system.

An intrinsically discrete approach is introduced in [11] for origami metamaterials, considering both in-plane affine, see also [33], and folding/bending deformation of facets, see [34, 35, 3, 7, 4] as well as inertial forces.<sup>6</sup> Potential walls on the strain energy, aiming to set impenetrability constraint on the folding energy, are introduced in [37].

In K-tube the basic elements that should be considered to build kinetic and strain energies are: i) a triangle moving in the three-dimensional space, which has an associated in-plane affine deformation energy and an associated kinetic energy and ii) a panel, i.e. two triangles sharing a side, which a folding energy is associated to.

In the approach employed in this work, which is an energy one, the strain energy is indeed additively split into two contributions: one accounting for in-plane affine deformation of facets and one accounting

<sup>&</sup>lt;sup>6</sup>For a primer in the dynamics of metamaterials see [36, 6].

for their folding around creases. In formulas, we assume the following expression for the stretching energy associated to a side, say the k-th

$$S_k = \frac{1}{2} a_k L_k g_k^2 \,, \tag{3}$$

where  $a_k$  is obtained as the product between Y, the Young modulus of the base material the K-tube is made up of, and  $A_k$ , the cross-sectional area of a fictitious rod placed along the k-side, while  $g_k$  is the Green strain measure of the k-side, i.e.

$$g_k = \frac{\ell_k^2 - L_k^2}{2L_k^2} \,. \tag{4}$$

We remark that the only quantity to be defined is  $A_k$ , which can be computed through a simple reasoning based onto an idea described in [33] and carried out in extended form in [11], where the interested reader will find the details.

Concerning the folding strain energy, its basic contribution is based on the change of the dihedral angle  $\delta$  in-between two triangles sharing a side. If we consider again the k-side, we assume for the folding strain energy the elementary contribution

190

205

$$F_k = \frac{1}{2} b_k L_k (\delta - \delta_0)^2 \,, \tag{5}$$

where  $b_k$  is the stiffness parameter which rules the relative rotation in-between the two considered triangles and  $\delta_0$  is the dihedral angle corresponding to the initial configuration. The stretching and folding strain energies of the whole K-tube are then evaluated by simply summing each single contribution. For more details we redirect the interested reader to the work [11], where a detailed definition of strain and kinetic energies associated to K-tube metamaterials is presented and to [37] for the introduction of potential walls in the strain energy related to the folding.

It remains to define an algorithm for the reconstruction of the dynamical evolution of the time-continuous discrete system originating from the modelling of the considered K-tube. In the technical literature there exist several methods to reconstruct the dynamical evolution of multi-degree-of-freedom systems, all having their peculiarities. The interested reader can find in the textbook [38] a clear introduction to the field, including a synoptic view over the main methods used to tackle the analysis of multi-degree-of-freedom systems and several related references.

In this work, we have implemented a numerical stepwise procedure initially proposed by Casciaro, see [39], thoroughly described in [40] and improved in [11]. In synthetic terms, when the time t is discretised into intervals of size  $\Delta t$ , the discrete-form impulse-momentum theorem can be written as

$$\mathbf{M}(\dot{\mathbf{u}}_{j+1} - \dot{\mathbf{u}}_j) + \left( \left( \frac{1}{2} - \alpha \right) (\mathbf{s}_j - \mathbf{f}_j) + \left( \frac{1}{2} + \alpha \right) (\mathbf{s}_{j+1} - \mathbf{f}_{j+1}) \right) \Delta t = \mathbf{0},$$
 (6)

where the mass matrix  $\mathbf{M}$  and the change of velocity  $\dot{\mathbf{u}}_{j+1} - \dot{\mathbf{u}}_j$  between the time step  $t_j$  and  $t_{j+1}$  are employed. The first term of the equation above can be interpreted as a finite-difference approximation of the momentum rate, while the second term is the average net impulse. We remark that in the last term there are two weighting factors that are function of the parameter  $\alpha$ . These two factors rule the weight of the impulse at the beginning and at the end of the time interval, respectively.

It is clear that this set of nonlinear scalar equations alone is not enough to solve the original problem. Indeed, the unknowns are collected in the vectors  $\mathbf{u}_{j+1}$  and  $\dot{\mathbf{u}}_{j+1}$ , whose entries are, in total, double the number of the scalar components of the impulse-momentum equation. In order to make equal equations and unknowns, Casciaro's scheme interpolates in time the displacements by means of a quadratic law involving the displacement at the beginning of the time step and its rates, *i.e.*, the corresponding velocities, at the beginning and at the end of the time step, in formulas

$$\mathbf{u}_{j+1} = \mathbf{u}_j + \left( \left( \frac{1}{2} - \beta \right) \dot{\mathbf{u}}_j + \left( \frac{1}{2} + \beta \right) \dot{\mathbf{u}}_{j+1} \right) \Delta t.$$
 (7)

We remark that: i) this kind of interpolation is a quadratic B-spline interpolation, see [41] and [42] for an application of this interpolation to finite elements in two and three space dimensions, respectively, and is the basis of Non-Uniform Rational Basis Splines, see, e.g., [43]; ii) also in the formula above two weighting factors depending on the parameter  $\beta$  appear. We remark that one can use Eq. 7 to eliminate the unknown vector  $\dot{\mathbf{u}}_{j+1}$  in Eq. 6, so as to have a system of N equations in the N unknowns collected in the vector  $\mathbf{u}_{j+1}$ .

We shall now discuss the choice of the parameters  $\alpha$  and  $\beta$ . To this end, we remind that Casciaro proposes in [39] some explicit formulas for computing  $\alpha$  and  $\beta$  in order to: i) make the solution stable; ii) eliminate instabilities due to roundoff errors; iii) eliminate the phenomenon of beat between spurious solutions. By referring to [40] for a careful analysis of Casciaro's method and the correction of some typos contained in [39], here we limit ourselves to remark that the main advantage of Casciaro's scheme is its adaptability to the time step size  $\Delta t$ . Indeed, on the one hand, to have a good accuracy this last cannot be chosen arbitrarily, but should be chosen sufficiently small, on the basis of the loading law and on the basis of the value taken by some quantities associated to the problem under consideration, like the first and last natural periods. On the other hand, very small time step sizes can be detrimental for computational time issues.

## 4. Numerical results

Analytical and numerical results presented in Sec. 2 were interesting enough to make us perform additional numerical simulations based on the same data, hence including the possible exhibition of bistable behaviour, in order to build some reference results which could help in outlining some guidelines for the construction of a simplified model of Kresling tube metamaterials. These simulations are complimentary to those presented in [9, 37] since these last, due to the employed geometrical data and a/b stiffness ratio, i.e., the ratio between the stiffness parameters a – which rules the stretching – and b – which rules the folding – could not observe any bistable behaviour.

Below, we present and discuss a series of selected simulation results which pave the way towards a continuum model of long K-tubes. Specifically, we explore the relationship between the kinematical quantity representing macroscopically the deformation of the K-tube, i.e. the variation of total height  $\Delta H$ , and the rotation and dilation/contraction of the polygonal cross-section of the K-tube. For those K-tubes which will be termed as long K-tubes, some tests aimed at characterising buckling load and post-buckling behaviour will be presented and discussed.

4.1. Four-stage K-tube subjected to axial shortening and lengthening. Making use of the same numerical data and geometry of the single-stage K-tube test – stiffness ratio  $a/b = \infty$  – the four-stage K-tube in Fig. 8 was considered, with total height equal to H = 4h. At first, two numerical simulations are presented, with prescribed axial shortening and lengthening, respectively. Two videoclips associated to these tests, showing the shape evolution of the K-tube, can be found in the supplementary material of this paper. By watching these videoclips it is possible to clearly see that, in shortening, the transition among two stable states for each stage occurs sequentially – starting from the bottom – while, in lengthening, this seems not occurring.

Figure 9 reports the rotation and stenosis of the cross-section of the four-stage K-tube in shortening (a) and lengthening (b). Plots in blue show the ratio between the rotation angle  $\Delta \vartheta$  and the angle  $\vartheta_0$ , from the first to the fourth stage – measured by probing the displacement evolution of the nodes 16, 23, 30 and 37, respectively, see Fig. 2(b) – versus the dimensionless relative shortening  $\Delta H/H$ . Plots in red show the radial strain, *i.e.* the ratio between the radius change  $\Delta R$  and the initial radius R of the polygonal cross-sections, versus the prescribed dimensionless vertical displacement  $\Delta H/H$ .

Concerning the two diagrams in Fig. 9, it can be remarked that:

- (1) because of the non-symmetric kinematic conditions there is a specific order in the occurrence of bistability in each stage in shortening;
- (2) in the shortening test, the cross-section rotation, depicted in blue, is practically linear for the top of the K-tube and, although less evident, it is also so for the other stages;<sup>9</sup>
- (3) in the shortening test, the stenosis, depicted in red, exhibits a behaviour similar to that reported in Fig. 6, namely an increase followed by a decrease, until reaching a null value, and again an increase that, this time, is practically linear;

This preprint research paper has not been peer reviewed. Electronic copy available at: https://ssrn.com/abstract=4783149

235

265

270

<sup>&</sup>lt;sup>7</sup>The key ingredient of the unconventional phenomenon producing stenosis of Kresling tubes, both when they are subjected to compression or traction – see [9, 37] – is that the ratio a/b is not high enough otherwise the bistable behaviour is not observable.

<sup>&</sup>lt;sup>8</sup>We refer to the videoclips K8x4h-b0-shortening and K8x4h-b0-lengthening.

<sup>&</sup>lt;sup>9</sup>The jumps in the diagrams, both for shortening and lengthening, originate from the fact that the routine developed to compute the rotation angle  $\Delta \theta$  assumes that  $\Delta \theta$  belongs to the interval  $[-\pi, \pi]$ .

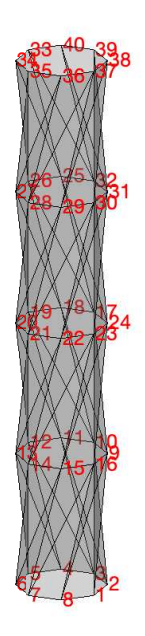


FIGURE 8. Four-stage K-tube 3D view.

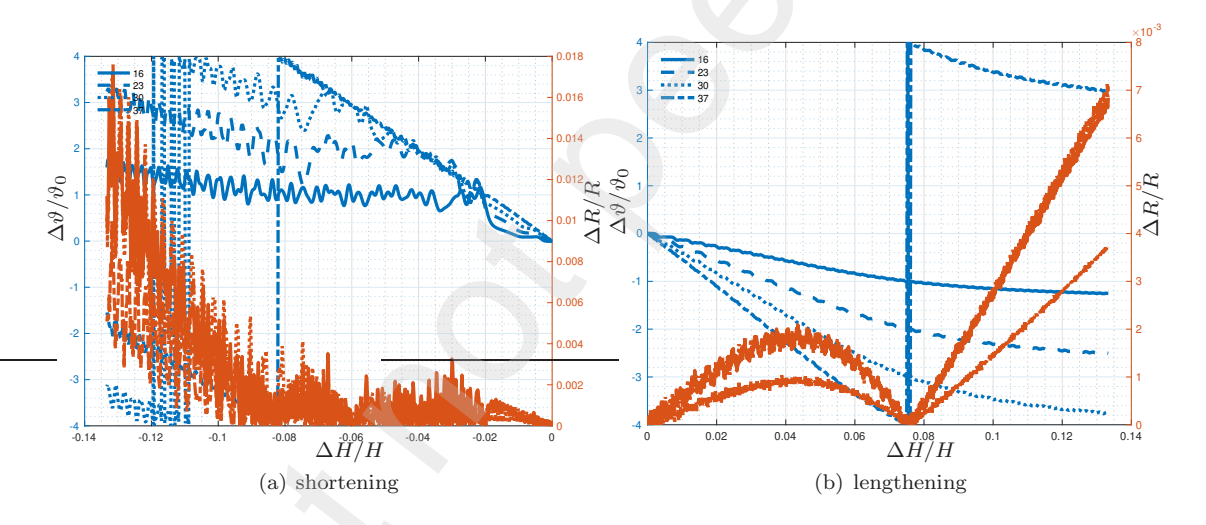


FIGURE 9. Four-stage K-tube subjected to axial shortening (a) and lengthening (b) tests. Normalised rotation and stenosis vs. normalised prescribed axial displacement for stage 1, 2, 3, and 4.

(4) in the lengthening test it is instead possible to recognise *i*) a nonlinear evolution of the cross-section rotation, depicted in blue and that *ii*) the behaviour of the radial strain, which initially increases, reaches a maximum, then decreases reaching a null value and, finally, increases in an almost linear way.

For the shortening case only we report in Fig. 10(a), as done in the previous section, the time evolution of the vertical reactions at the top nodes. It can be remarked that all the curves perfectly overlap in the initial time period while they subsequently differ as soon as the top octagon rotates besides translating and loss of stability is observed. Figure 10(b) shows the Euclidean norm of the reaction vector against the Euclidean norm of the displacement vector. It clearly shows that, except for oscillations due to the consideration of inertial forces, the norm of the reaction vector exhibits a piece-wise linear behaviour in

time: a first (practically) linear part with a low slope is followed by a linear part characterised by an extremely high slope.

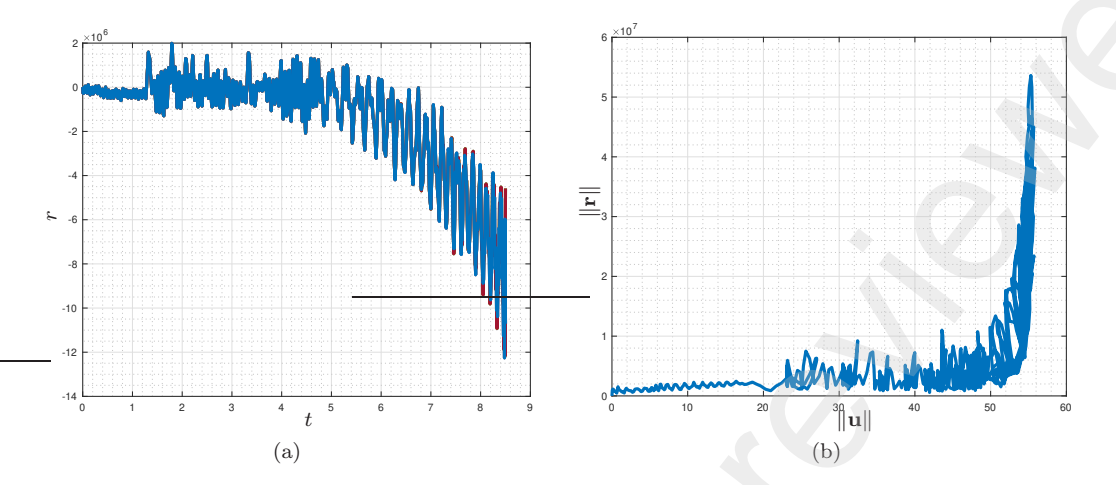


FIGURE 10. Four-stage K-tube subjected to an axial shortening test. Time evolution of the vertical reaction r of the top nodes (a) and norm  $\|\mathbf{r}\|$  of the reaction vector vs. the displacement vector norm  $\|\mathbf{u}\|$ .

4.2. Twenty-stage K-tube subjected to axial shortening and lengthening. In this section, we shall discuss the results obtained by performing simulations with a twenty-stage K-tube subjected to axial shortening and lengthening. Let us define the slenderness parameter  $\lambda$  as the ratio between the length H and the diameter of the K-tube. Considering the K-tube obtained by superimposing 20 stages having the same geometrical data employed so far, we obtain the value  $\lambda = 30$ . Figure 11 shows a three-dimensional view of the considered K-tube. Because of its high slenderness, we expect the mechanical behaviour of the considered K-tube to be, roughly speaking, similar to that exhibited by a classical beam.

Figure 12 reports the first nine natural periods and modes for the ratio  $a/b = \infty$ . We remark that this first group of modes includes two deformed shapes suggesting that the stenosis of K-tubes is an intrinsic characteristic of this kind of tubes, which seems a reasonable fact for K-tubes with negligible stored folding energy.

For the shortening test Fig. 13(a) reports the curves representing the time evolution of the displacement coordinates of the 168-th node, one of the top nodes, while Fig. 13(b) reports the time evolution of kinetic, stretching and folding strain energies for the whole tube, this last being null in the analysed test. Figure 13(c) reports the normalised rotation and the radial strain against the prescribed non-dimensional axial shortening. These plotted quantities are computed by probing the transverse displacement of nodes 142, 148, 154, and 168, a set of nodes such that each belongs to one of the four top stages and such that they are all lying on the same vertical line. It is remarkable that, as expected, as the number of stages increases the plots concerning adjacent stages become more and more close to each other, a behaviour suggesting that a homogenisation result can be sought.

Figure 14 shows the time evolution of the vertical structural reactions of the top nodes, which are again perfectly overlapping until slightly more than ten seconds from the initial time, revealing thereafter the occurrence of buckling. The same conclusions can be drawn looking at Fig. 14(b), which reports the structural reaction vector norm versus the displacement vector norm. The videoclip K8x20h-b0.mp4 included in the supplementary materials shows the complete pre- and post-buckling path observed from the top and lateral standpoints, as well as with a 3D view, along with the time evolution of the displacement vector norm. Some stroboscopic shoots are reported in Fig. 15, showing the buckling behaviour of the considered K-tube.

4.3. What changes when folding energy is considered? We now seek to understand what is the change in the previous results brought by taking into account the folding energy. The first test here analysed concerns the four-stage K-tube subjected to prescribed axial shortening. As said, we introduce



FIGURE 11. Twenty-stage K-tube 3D view.

a nonzero folding stiffness b and, specifically, we choose the ratio  $a/b = 10^5$ , as for the single-stage K-tube test, which assures from both a mechanical and geometrical standpoint that each stage of the K-tube can exhibit bistability.

First of all, we observe that the natural periods computed for the reference configuration are practically unchanged with respect to the case with  $a/b = \infty$  examined in the foregoing. The numerical simulations performed by tuning the employed time-integration scheme according to the preliminary eigenvalues analysis, lead us to the plots reporting the time evolution of the displacement coordinates of the 37-th node and the energies for the whole tube – kinetic, stretching and folding contributions – in Fig. 16.

From these plots we conclude that the introduction of the folding energy contribution makes less steep the variation in time of the total strain energy, namely stretching plus folding.

The second analyzed test considers a twenty-stage K-tube with the same geometrical data and boundary conditions chosen for the previous test. The only difference lies in the choice of the ratio  $a/b=10^5$ , which allows for bistability of each stage of the K-tube. The first remark concerns the natural periods and modes which, also in this case, remain practically unchanged with respect to those reported in Fig. 12 for the ratio  $a/b=\infty$ .

Figure 17, see Fig. 13 for comparison, reports the time evolution of the displacement coordinates of node 168 (a), that of the energies (b) – kinematic, stretching and folding – along with the dimensionless rotation and stenosis against the dimensionless relative vertical displacement. These last two plotted quantities are computed by probing the transverse displacement of nodes 142, 148, 154, and 168, a set of nodes such that each belongs to one of the four top stages and such that they are all lying on the same vertical line.

Likewise to the case considering the stiffness ratio  $a/b = \infty$ , we report in Fig. 18(a) the curves representing the vertical displacement coordinates of the top nodes, which also in this case are perfectly overlapping until slightly more than four seconds, when buckling onset occurs. The same conclusions can

be drawn by looking at Fig. 18(b), which reports the structural reaction vector norm against the displacement vector norm. A short videoclip included in the supplementary materials – K8x20h-c-aonb1e5.mp4 – shows the complete buckling path from several views along with the time evolution of the displacement vector norm.

4.4. **Displacement-controlled shearing tests.** In this subsection we take into account a K-tube with, again, eight sides and four stages. We perform some simulations to study the mechanical behaviour of this K-tube subjected to prescribed shearing displacement to the top of the tube for different values of the folding stiffness coefficient b. Specifically, we consider the ratios  $a/b = \infty$ ,  $a/b = 10^5$ , and  $a/b = 10^3$ . As proven above, the first two ratios ensure the possibility of bistable mechanical behaviour of each stage, while the third ratio precludes bistability, since the folding energy is too significant with respect to the stretching energy. Besides that, we also investigate the possible transversely anisotropic behaviour that could be induced by the non-circularity of the cross-section. Some simulations obtained by varying the direction of the prescribed transverse displacement for  $a/b = \infty$ ,  $a/b = 10^5$ , and  $a/b = 10^3$  are performed and their results discussed.

Figure 19 shows the time evolution of the displacement coordinates of the 37-th node for  $a/b = \infty$  (a),  $a/b = 10^5$  (b), and  $a/b = 10^3$  (c); energies are reported for the same stiffness ratios in (d), (e), and (f). Figure 20 reports three polar plots showing the time evolution of the norm of the vector collecting all the vertical displacements of the K-tube varying the direction of the given horizontal displacement. We observe that increasing the folding stiffness b reduces the anisotropy that, in all analysed case studies, does not seem anyway relevant.

## 5. CONCLUDING REMARKS AND FUTURE CHALLENGES

In this paper we have presented the results of some numerical simulations concerning Kresling tube metamaterials – with one, four, and twenty stages – characterised by geometry and stiffnesses capable of conferring to them bistability behaviour. Shortening, lengthening, and shearing tests, this last along different directions, have been considered.

We have attempted at elucidating an exotic feature of the mechanical behaviour of K-tubes, namely a special buckling mode consisting in a stenosis, which is observed in axial lengthening tests, see [9], thus widening the number of problems for which buckling is observed under axial lengthening [44, 45]. We have proved that, besides the geometry and its dimensions, to obtain such a buckling behaviour it is crucial to have a proper ratio between the stiffnesses which rule the stretchability of each facet constituting the K-tube and the folding of two adjacent facets around the shared crease. The understanding provided by the modelling methodology utilised in this paper can be combined with an optimisation procedure like that proposed in [46], leading to designing K-tube exhibiting up to a desired extent and under desired conditions this special buckling mode.

The presented and discussed numerical simulations pave the way towards the conception of homogenised model adapt for long K-tubes. The development of one- or two-dimensional simplified continuum models, through a suitable homogenisation process, should embed the coupling between shortening/lengthening and the consequent cross-sectional rotation (around the tube axis) and, possibly, the K-tube stenosis. All these phenomena should be taken into account in a one-dimensional model through additional kinematic parameters.

We also remark that Kresling tube metamaterials constituted by several stages and, possibly, proportionally many facets in a single stage, deserve to be explored from the mechanical point of view since, when the triangles can be considered as unstretchable, their behaviour is caught by the so-called sine-Gordon equation, which, in turn, has the relevant characteristic of possessing a solitary wave solution.

In addition, future developments and challenges include the physical realisation of K-tubes by means of 3D printing processes and the subsequent mechanical testing. Regarding the physical realisation of K-tubes by means of 3D printing, it would be interesting to attempt at designing extremely compliant micro-structured facets, exploiting, as an instance, the pantographic motif. Facets might have a bi-pantographic [47] microstructure. Furthermore, experimental campaigns could be focused on the assessment of different 3D-printing processes and raw materials in the manufacturing of K-tubes, in that they affect the mechanical and morphological properties of printed samples [48]. To this end, the use of Digital Image Correlation (DIC) and Digital Volume Correlation (DVC) is envisaged, as they now constitute a consolidated tool to analyse kinematic details in experiments performed on metamaterials, a

task that cannot be easily achieved by means of more classical measurement techniques like strain gauges or extensometers [49, 50, 51].

#### Acknowledgement

Emilio Turco gratefully acknowledges the support of the University of Sassari (Fondo di Ateneo per la ricerca 2020). The research reported in the present contribution was carried out as part of the project Metamaterials design and synthesis with applications to infrastructure engineering funded by the MUR Progetti di Ricerca di rilevante Interesse Nazionale (PRIN) Bando 2022 - grant 20228CPHN5.

## APPENDIX A. A NOTE ON K-TUBES AND THEIR PATTERN

We consider the planar folding pattern required to get a single-stage K-tube based on a regular polygon with N sides inscribed in a circle of centre O and radius R. The pattern is completely described in terms of the side length  $\ell$ , the height h and the gap g, in addition to the number of sides N, see the upper part of Fig. 21. We want to determine the geometrical properties of the K-tube in its initial configuration from those of the pattern, considering that the initial zero-energy configuration of the K-tube is obtained by a transformation of the pattern that keeps unaltered the creases' lengths.

Each stage of the K-tube is obtained by rotating about the tube axis the top polygon with respect to the bottom polygon of an angle  $\vartheta_0$ . At first, let us define the quantity  $\alpha = 2\pi/N$ . Since the length  $\ell$  can be expressed as  $\ell = 2R\sin(\alpha/2)$ , we have the following relation between the radius R and the angle  $\alpha$ :

$$R = \frac{\ell}{2\sin\frac{\alpha}{2}}. (8)$$

Looking at the lower part of Fig. 21, which refers to the top polygon with N sides, we consider the (N+1)-th node before and after the rotation of amplitude  $\vartheta_0$ , around the K-tube axis (O') is the intersection of the rotation axis with the plane containing the top nodes of the K-tube). Having denoted with  $\overline{\mathbf{X}}_{N+1}$  the initial position – before the rotation of an angle  $\vartheta_0$  – and with  $\mathbf{X}_{N+1}$  the final position – after the rotation – of this node, it is immediate to link the distance g with the radius R and the angle  $\vartheta_0$ . In formulas, we have

$$\vartheta_0 = 2\arcsin\frac{g}{2R} \,. \tag{9}$$

At this point we have all the quantities to define the vectors  $\mathbf{X}_1$  and  $\mathbf{X}_{N+1}$ . In explicit form, we can write

$$\mathbf{X}_{1} = \begin{bmatrix} R \\ 0 \\ 0 \end{bmatrix}, \qquad \mathbf{X}_{N+1} = \begin{bmatrix} R\cos\theta_{0} \\ R\sin\theta_{0} \\ H \end{bmatrix}, \tag{10}$$

and, as a consequence

405

415

420

425

$$\|\mathbf{X}_{N+1} - \mathbf{X}_1\| = \sqrt{R^2(\cos\vartheta_0 - 1)^2 + R^2\sin^2\vartheta_0 + H^2}.$$
 (11)

Since 
$$\|\mathbf{X}_{N+1} - \mathbf{X}_1\| = \sqrt{g^2 + h^2}$$
, we can compute  $H$  as
$$H = \sqrt{g^2 + h^2 - R^2 \left( \left( \cos \vartheta_0 - 1 \right)^2 + \sin^2 \vartheta_0 \right) \right)},$$
(12)

which, as it is straightforward to verify, is identical to h.

# References

- [1] E. Turco. Discrete is it enough? The revival of Piola-Hencky keynotes to analyze three-dimensional Elastica. Continuum Mechanics and Thermodynamics, 30(5):1039-1057, September 2018.
- [2] E. Turco. Modeling of three-dimensional beam nonlinear vibrations generalizing Hencky's ideas. Mathematics and Mechanics of Solids, 27(10):1950-1973, January 2022.
- [3] E. Turco, E. Barchiesi, I. Giorgio, and F. dell'Isola. A Lagrangian Hencky-type non-linear model suitable for metamaterials design of shearable and extensible slender deformable bodies alternative to Timoshenko theory. International Journal of Non-Linear Mechanics, 123:103481, April 2020.
- [4] E. Turco. In-plane shear loading of granular membranes modeled as a Lagrangian assembly of rotating elastic particles. Mechanics Research Communications, 92:61-66, 2018.

440

445

480

485

- [5] E. Turco, F. dell'Isola, and A. Misra. A nonlinear Lagrangian particle model for grains assemblies including grain relative rotations. International Journal for Numerical and Analytical Methods in Geomechanics, 43(5):1051–1079, 2019.
  - [6] E. Turco. Forecasting nonlinear vibrations of patches of granular materials by elastic interactions between spheres. Mechanics Research Communications, 122(103879):1–5, March 2022.
  - [7] E. Barchiesi, F. dell'Isola, A. M. Bersani, and E. Turco. Equilibria determination of elastic articulated duoskelion beams in 2D via a Riks-type algorithm. *International Journal of Non-Linear Mechanics*, 128(103628):1–24, January 2021.
  - [8] E. Turco, E. Barchiesi, and F. dell'Isola. In-plane dynamic buckling of duoskelion beam-like structures: discrete modeling and numerical results. *Mathematics and Mechanics of Solids*, 27(7):1164–1184, 2022.
  - [9] E. Turco, E. Barchiesi, A. Causin, F. dell'Isola, and M. Solci. Kresling tube metamaterial exhibits extreme largedisplacement buckling behavior. Mechanics Research Communications, 134(104202):1-7, 2023.
  - [10] K. Liu and G. H. Paulino. Nonlinear mechanics of non-rigid origami: an efficient computational approach. Proceedings of the Royal Society A: Mathematical, Physical and Engineering Sciences, 2017.
  - [11] E. Turco, E. Barchiesi, and F. dell'Isola. Nonlinear dynamics of origami metamaterials: energetic discrete approach accounting for bending and in-plane deformation of facets. Zeitschrift für Angewandte Mathematik und Physik (ZAMP), 74(26):1–29, 2023.
  - [12] A. E. Forte amd D. Melancon, M. Zanati, M. De Giorgi, and K. Bertoldi. Chiral mechanical metamaterials for tunable optical transmittance. *Advanced Functional Materials*, (2214897):1–7, 2023.
  - [13] Q. Ze, S. Wu, J. Nishikawa, J. Dai, Y. Sun, S. Leanza, C. Zemelka, L. S. Novelino, G. H. Paulino, and R. R. Zhao. Soft robotic origami crawler. *Science Advances*, 8(eabm7834):1–9, March 2022.
- [14] J. Kaufmann, P. Bhovad, and S. Li. Harnessing the multistability of Kresling origami for reconfigurable articulation in soft robotic arms. Soft Robotics, doi: 10.1089/soro.2020.0075:1-12, 2021.
  - [15] Y. Kim and Y. Cha. Soft pneumatic gripper with a tendon-driven soft origami pump. Frontiers in Bioengineering and Biotechnology, 8, 2020.
  - [16] K. Chong, E. Pertigkiozoglou, C. Saad, and A. Stack. 8twist, Fall 2017.
- 455 [17] K. Kuribayashi, K. Tsuchiya, Z. You, D. Tomus, M. Umemoto, T. Ita, and M. Sasaki. Self-deployable origami stent grafts as a biomedical application of Ni-rich TiNi shape memory alloy foil. *Materials Science Engineering A*, 419:131– 137, 2006.
  - [18] R. Masana, S. Khazaaleh, H. Alhussein, R. S. Crespo, and M. F. Daqaq. An origami-inspired dynamically actuated binary switch. Applied Physics Letters, 117(081901), 2020.
- [19] H. Yasuda, Y. Miyazawa, E. G. Charalampidis, C. Chong, P. G. Kevrekidis, and J. Yang. Origami-based impact mitigation via rarefaction solitary wave creation. Science Advances, 5(5):1–8, 2019.
  - [20] M. Al-Mansoori, K. A. Khan, and W.J. Cantwell. Harnessing architected stiffeners to manufacture origami-inspired foldable composite structures. *Composite Science and Technology*, 200(108449):1–11, 2020.
- [21] K. Liu, T. Tachi, and G. H. Paulino. Bio-inspired origami metamaterials with metastable phases through mechanical phase transitions. *Journal of Applied Mechanics, ASME*, 88(091002):1–10, 2021.
  - [22] Z. Chang, T. D. Tu, K. Narumi, and H. Kim. Kirigami haptic swatches: Design methods for cut-and-fold haptic feedback mechanisms. In CHI 2020, number 526, pages 1–12, Honolulu, HI, USA, April 2020. Association for Computing Machinery.
- [23] J. F. Abel and J. R. Cooke, editors. Deployable Structures and Biological Morphology. Proceedings of the 6th International Conference on Computation of Shell and Spatial Structures, 2008.
  - [24] K. Miura. Method of packaging and deployment of large membranes in space. Report 618, The Institute of Space and Astronautical Science, 1985.
  - [25] J. F. V. Vincent. Deployable structures in nature: potential for biomimicking. Proceedings of the Institution of Mechanical Engineers, Part. C: Journal of Mechanical Engineering Science, 214(1):1–10, 2000.
- 475 [26] S. Georgakopolous, E. Tentzeris, and B. Cook. Origami folded antennas. United States Patent n. US 9,214,722 B2, December, 15 2015.
  - [27] A. Braides and M. Solci. Asymptotic analysis of Lennard–Jones systems beyond the nearest-neighbour setting: a one-dimensional prototypical case. *Mathematics and Mechanics of Solids*, 21(8):915–930, 2016.
  - [28] R. Alicandro, A. Braides, M. Cicalese, and M. Solci. Discrete Variational Problems with Interfaces. Cambridge University Press, 2023.
    - [29] A. Braides, A. Causin, M. Solci, and L. Truskinovsky. Beyond the classical Cauchy–Born rule. Archive for Rational Mechanics and Analysis, 247(107):1–113, November 2023.
  - [30] R. Xu, C. Chen, J. Sun, Y. He, X. Li, M.-H-Lu, and Y. Chen. The design, manufacture and application of multistable mechanical metamaterials-a state-of-the-art review. *International Journal of Extreme Manufacturing*, 5(4):042013, 2023
  - [31] M. Schenk and S. D. Guest. Origami folding: A structural engineering approach. In Origami 5: Fifth International Meeting of Origami Science, Mathematics, and Education, Singapore, July 2011.
  - [32] M. Schenk and S. D. Guest. Geometry of miura-folded metamaterials. *Proceedings of National Academy of Science of the United States of America*, 110(9):3276–3281, February 2013.
- 490 [33] J. Argyris, L. Tenek, and L. Olofsson. TRIC: a simple but sophisticated 3-node triangular element based on 6 rigid-body and 12 straining modes for fast computational simulations of arbitrary isotropic and laminated composite shells. Computer Methods in Applied Mechanics and Engineering, 145:11–85, 1997.

- [34] H. Hencky. Über die angenäherte Lösung von Stabilitätsproblemen im Raum mittels der elastischen Gelenkkette. PhD thesis, Engelmann, 1921.
- 495 [35] E. Turco, F. dell'Isola, A. Cazzani, and N. L. Rizzi. Hencky-type discrete model for pantographic structures: numerical comparison with second gradient continuum models. Zeitschrift für Angewandte Mathematik und Physik, 67(85):1–28, August 2016.
  - [36] D. Del Vescovo and I. Giorgio. Dynamic problems for metamaterials: review of existing models and ideas for further research. *International Journal of Engineering Science*, 80:153–172, 2014.
- 500 [37] E. Turco, E. Barchiesi, A. Causin, F. dell'Isola, and M. Solci. Harnessing unconventional buckling of tube origami metamaterials based on Kresling pattern. *International Journal of Solids and Structures*, submitted, 2023.
  - [38] P. Wriggers. Nonlinear finite element methods. Springer, 2008.
  - [39] R. Casciaro. Time evolutional analysis of nonlinear structures. Meccanica, 3(X):156-167, 1975.
  - [40] E. Turco. Stepwise analysis of pantographic beams subjected to impulsive loads. *Mathematics and Mechanics of Solids*, 26(1):62–79, 2021.
  - [41] M. Aristodemo. A high-continuity finite element model for two-dimensional elastic problems. Computers & Structures, 21(5):987–993, 1985.
  - [42] A. Bilotta, G. Formica, and E. Turco. Performance of a high-continuity finite element in three-dimensional elasticity. International Journal for Numerical Methods in Biomedical Engineering, 26:1155–1175, 2010.
  - [43] A. Cazzani, M. Malagù, and E. Turco. Isogeometric analysis of plane curved beams. Mathematics and Mechanics of Solids, 21(5):562–577, 2016.
    - [44] V. A. Eremeyev and E. Turco. Enriched buckling for beam-lattice metamaterials. *Mechanics Research Communications*, 103(103458):1–7, January 2020.
  - [45] D. Zaccaria, D. Bigoni, G. Noselli, and D. Misseroni. Structures buckling under tensile dead load. *Proceedings of the Royal Society A: Mathematical, Physical and Engineering Sciences*, 467(2130):1686–1700, 2011.
  - [46] B. Desmorat, M. Spagnuolo, and E. Turco. Stiffness optimization in nonlinear pantographic structures. Mathematics and Mechanics of Solids, 25(11):2252–2262, 2020.
  - [47] E. Barchiesi, F. dell'Isola, F. Hild, and P. Seppecher. Two-dimensional continua capable of large elastic extension in two independent directions: Asymptotic homogenization, numerical simulations and experimental evidence. *Mechanics Research Communications*, 103:103466, 2020.
  - [48] M. De Angelo, M. Spagnuolo, F. D'annibale, A. Pfaff, Klaus Hoschke, Aviral Misra, Corinne Dupuy, Patrice Peyre, J. Dirrenberger, and M. Pawlikowski. The macroscopic behavior of pantographic sheets depends mainly on their microstructure: experimental evidence and qualitative analysis of damage in metallic specimens. *Continuum Mechanics* and *Thermodynamics*, 31:1181–1203, 2019.
- 525 [49] M. Valmalle, B. Smaniotto, M. Spagnuolo, A. Ciallella, and F. Hild. Mesoscale DVC analyses and parameter calibration for pantographic block in 3-point flexure. European Journal of Mechanics - A/Solids, 101(105063):1–14, 2023.
  - [50] P. Auger, T. Lavigne, B. Smaniotto, M. Spagnuolo, F. dell'Isola, and F. Hild. Poynting effects in panto-graphic metamaterial captured via multiscale DVC. The Journal of Strain Analysis for Engineering Design, doi: 10.1177/0309324720976625, 2020.
- 530 [51] M. Valmalle, A. Vintache, B. Smaniotto, F. Gutmann, M. Spagnuolo, A. Ciallella, and F. Hild. Local-global DVC analyses confirm theoretical predictions for deformation and damage onset in torsion of pantographic metamaterial. Mechanics of Materials, 172(104379):1–16, 2022.

Email address, corresponding author: emilio.turco@uniss.it

Email address: ebarchiesi@uniss.it

515

520

535 Email address: francesco.dellisola@univaq.it

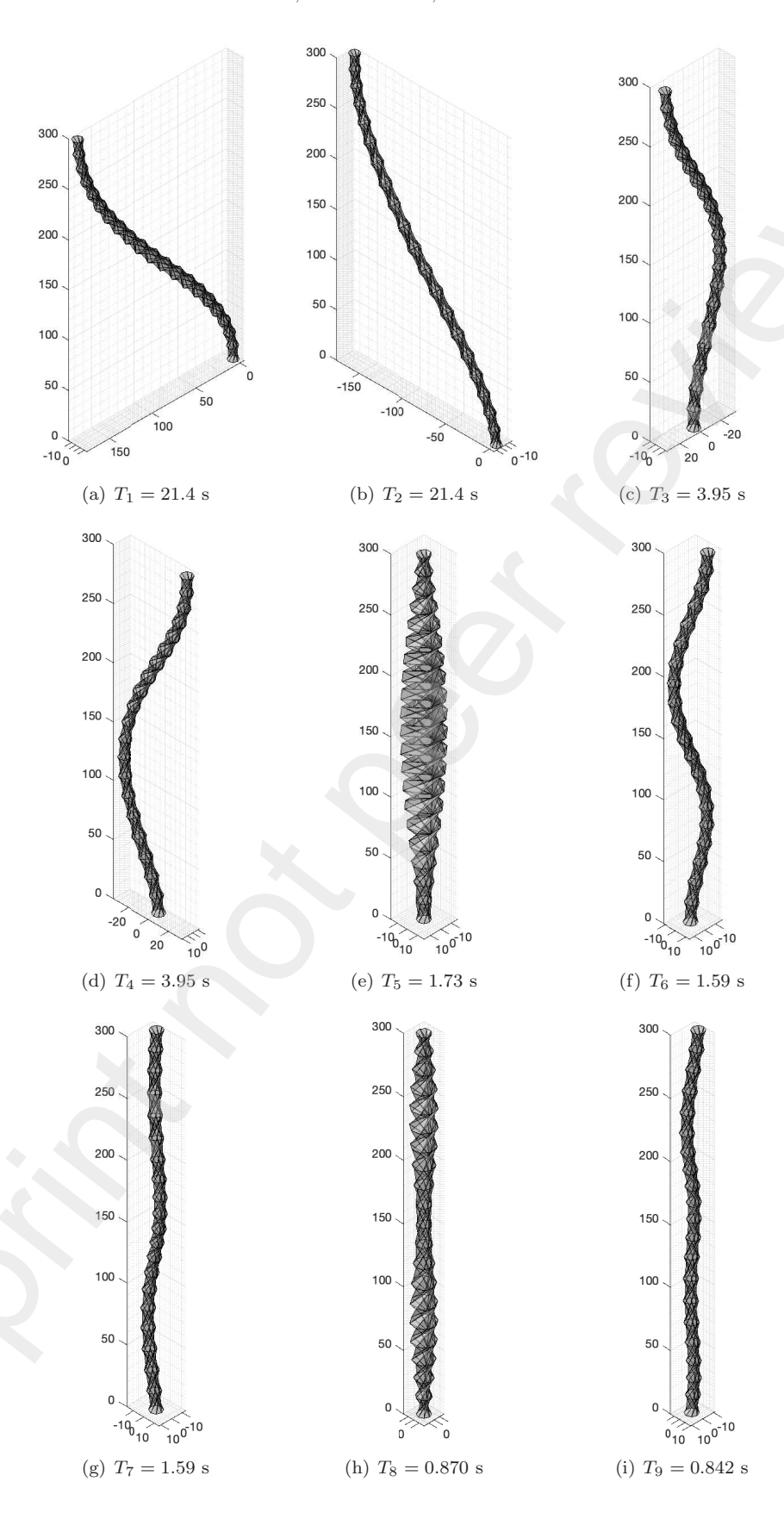


FIGURE 12. Twenty-stage K-tube. First nine natural periods and modes for the stiffness ratio  $a/b=\infty$ .

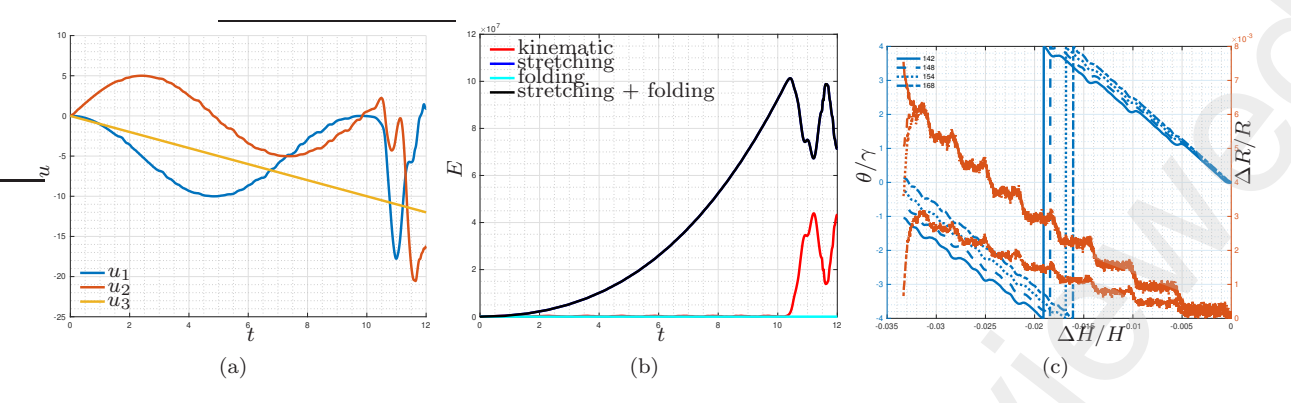


FIGURE 13. Twenty-stage K-tube with stiffness ratio  $a/b = \infty$ . Time evolution of the displacement coordinates of the 168-th node (a), time evolution of kinematic, stretching and folding energies for the whole tube (b), and rotation and radial stretching vs. vertical displacement for the four top stages (c).

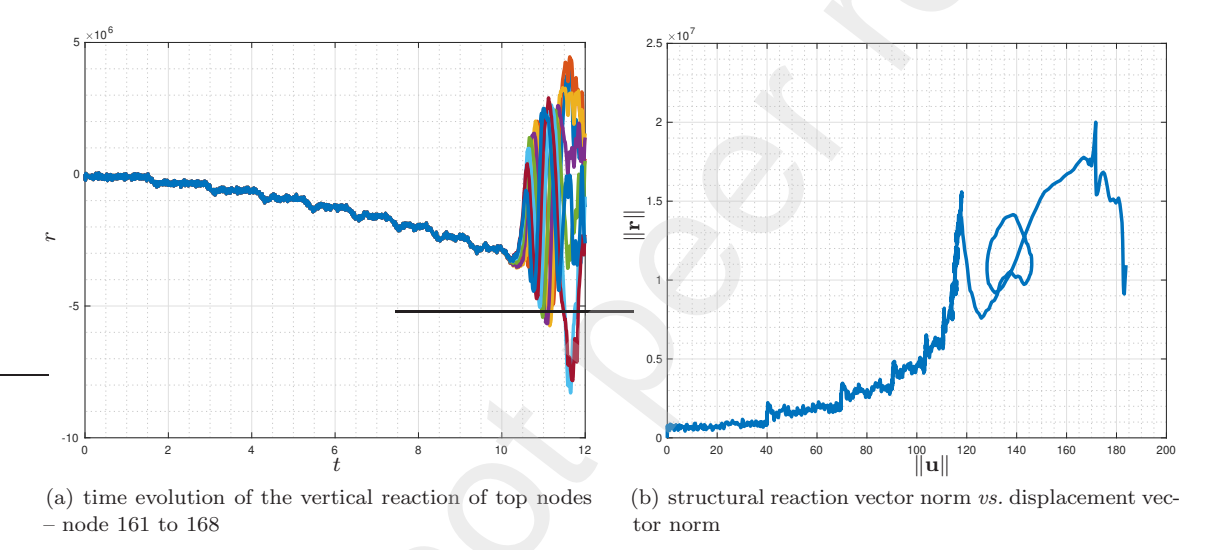


FIGURE 14. Twenty-stage K-tube with stifness ratio  $a/b = \infty$ . Time evolution of the vertical reaction of top nodes – from node 161 to 168 (a) and structural reaction vector norm vs. displacement vector norm (b).

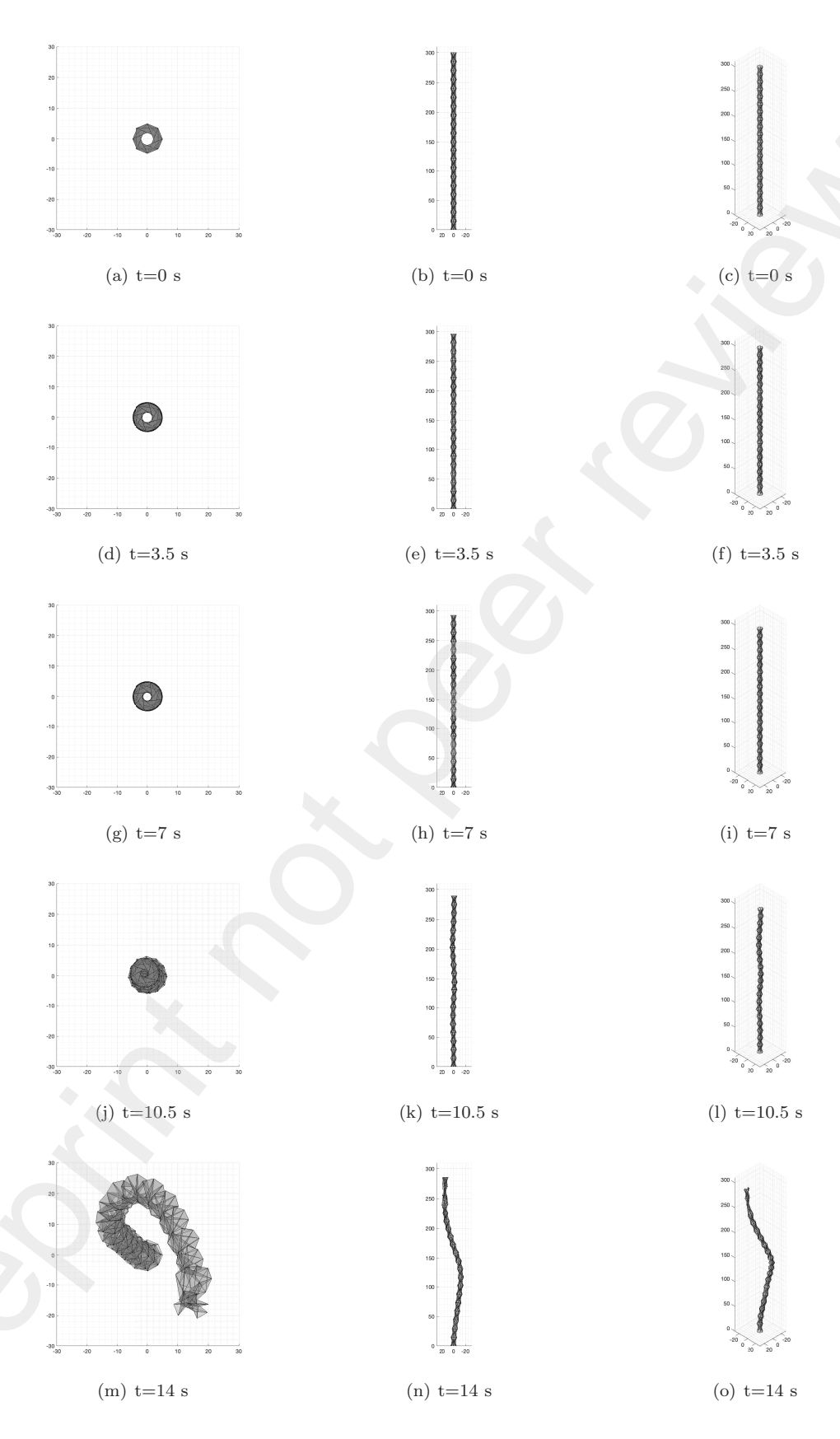


FIGURE 15. Twenty-stage K-tube with stiffness ratio  $a/b = \infty$ . Stroboscopic shoots in the time interval [0, 14] s. Top view on the left, side view on the center and 3D view on the right.

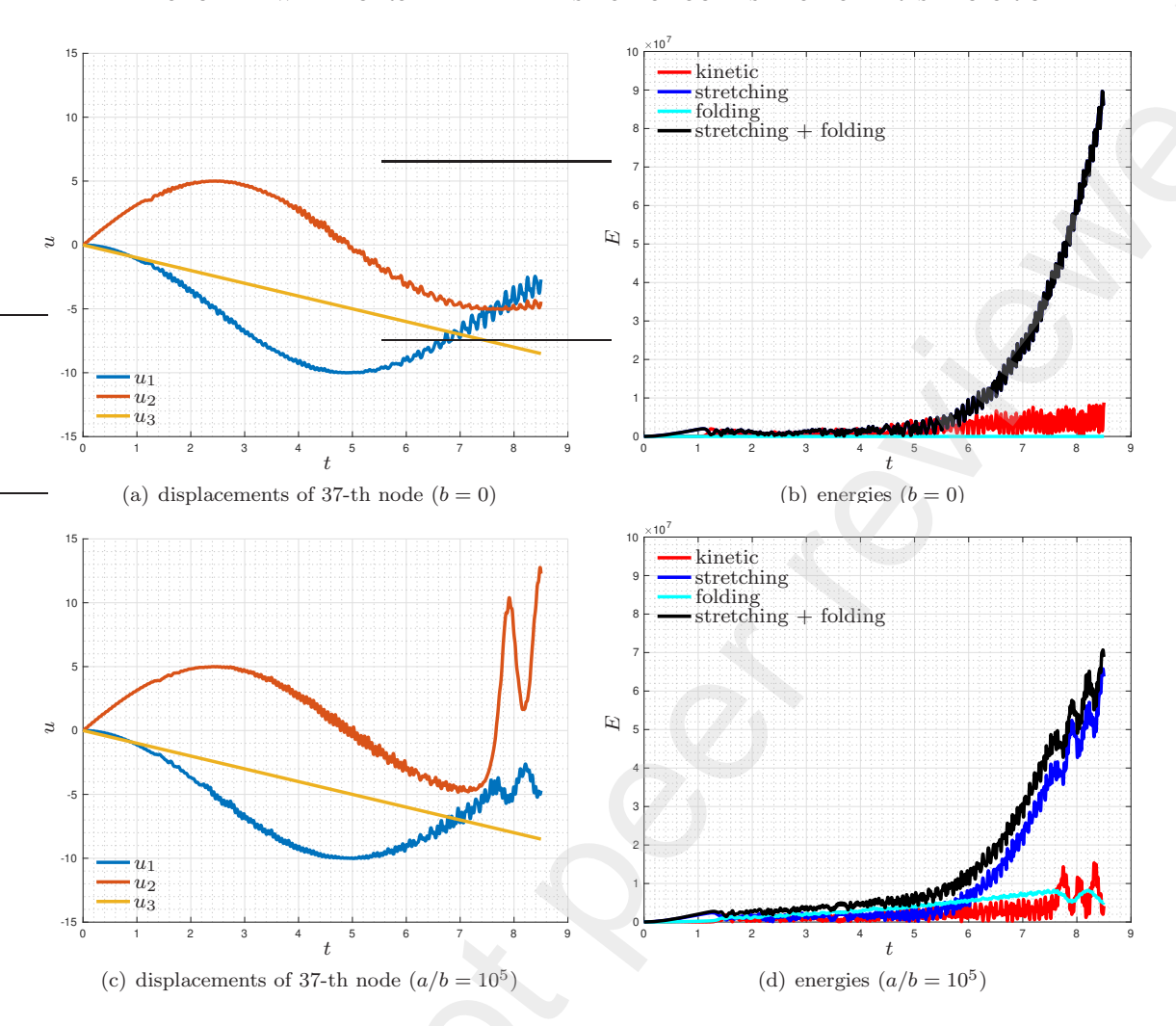


FIGURE 16. Four-stage K-tube subjected to prescribed axial shortening. Time evolution of the displacement coordinates of the 37-th node (a,c) and time evolution of energies (b,d) for stiffness ratios  $a/b = \infty$  and  $a/b = 10^5$ , respectively.

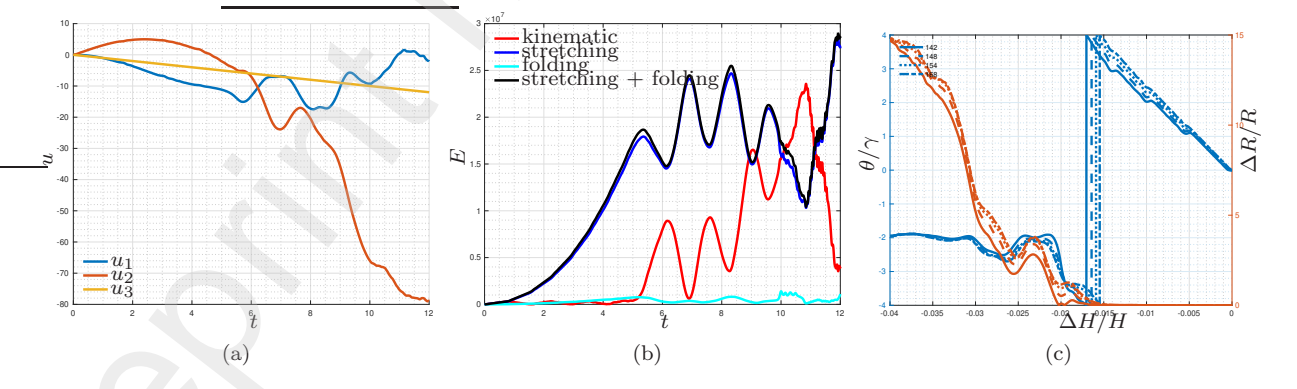
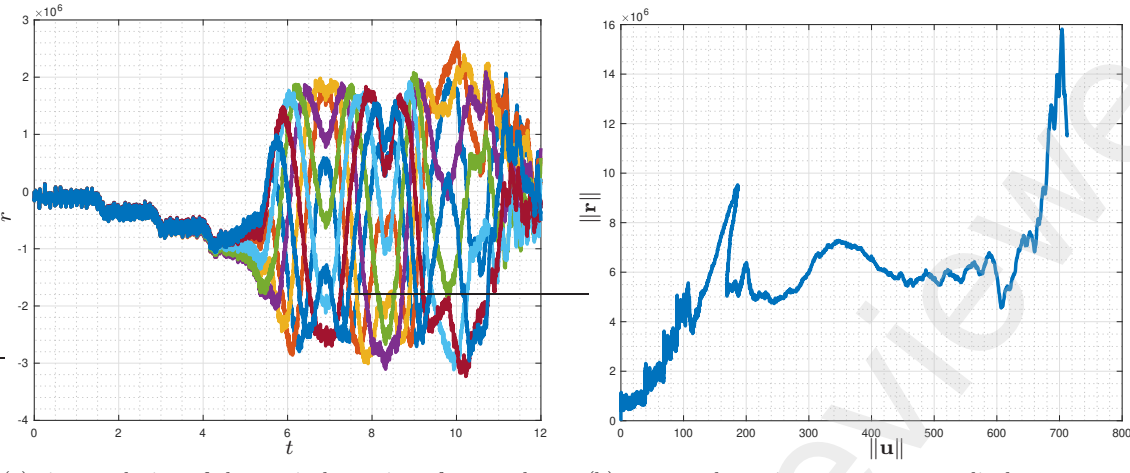


FIGURE 17. Twenty-stage K-tube with stiffness ratio  $a/b = 10^5$ . Time evolution of displacement coordinates of the 168-th node (a), time evolution of stretching, folding, and kinetic energies (b), and rotation and radial stretching vs vertical displacement for the top four stages.



- (a) time evolution of the vertical reaction of top nodes from node 161 to 168  $\,$
- (b) structural reaction vector norm vs. displacement vector norm

FIGURE 18. Twenty-stage K-tube with stiffness ratio  $a/b = 10^5$ . Time evolution of top nodes vertical reaction (a) and structural reaction vector norm vs. displacement vector norm (b).

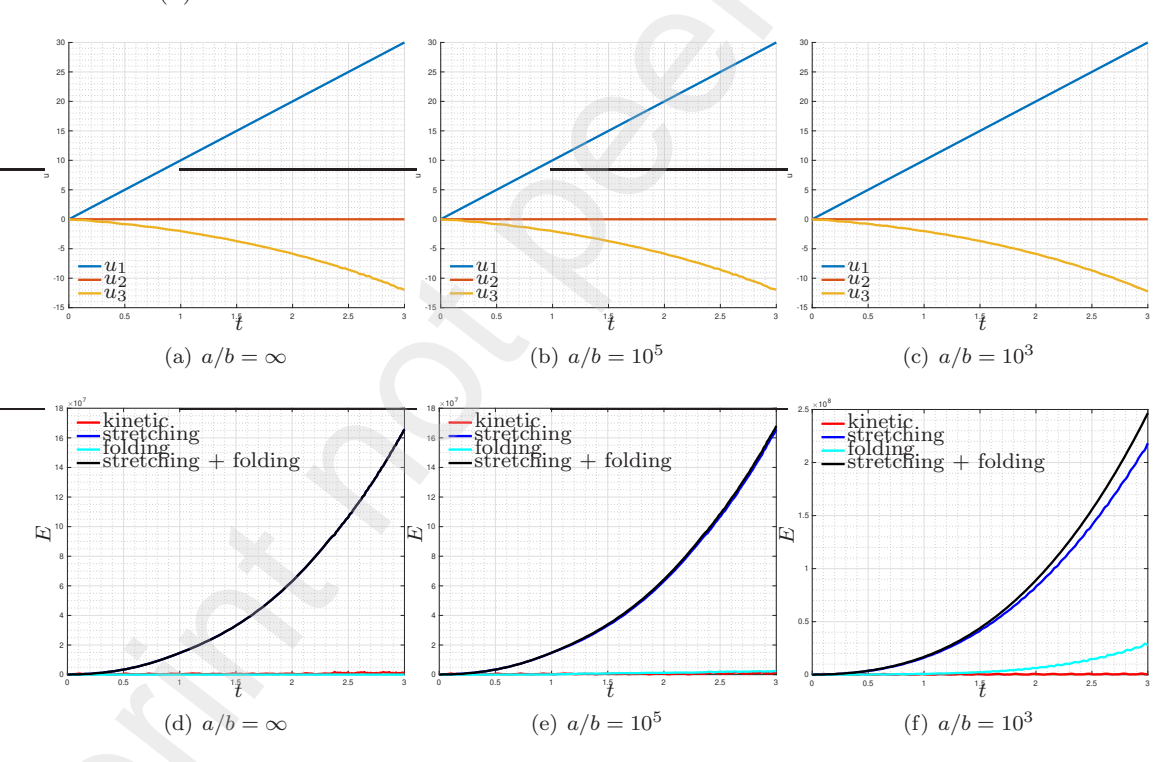


FIGURE 19. Four-stage K-tube subjected to shearing test. Time evolution of the 37-th node displacement (a),(b) and (c) and time evolution of energy (d), (e) and (f) for cases  $a/b=\infty$ ,  $a/b=10^5$  and  $a/b=10^3$ .

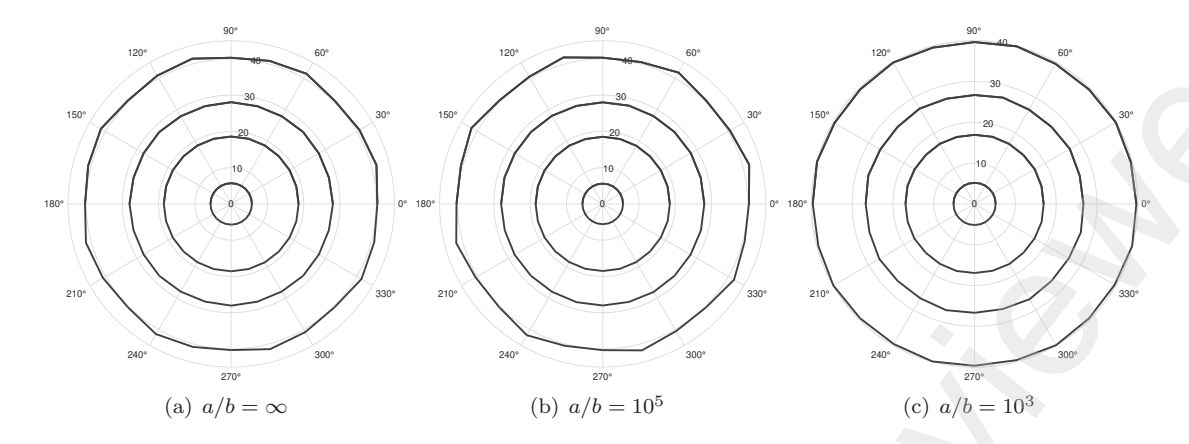
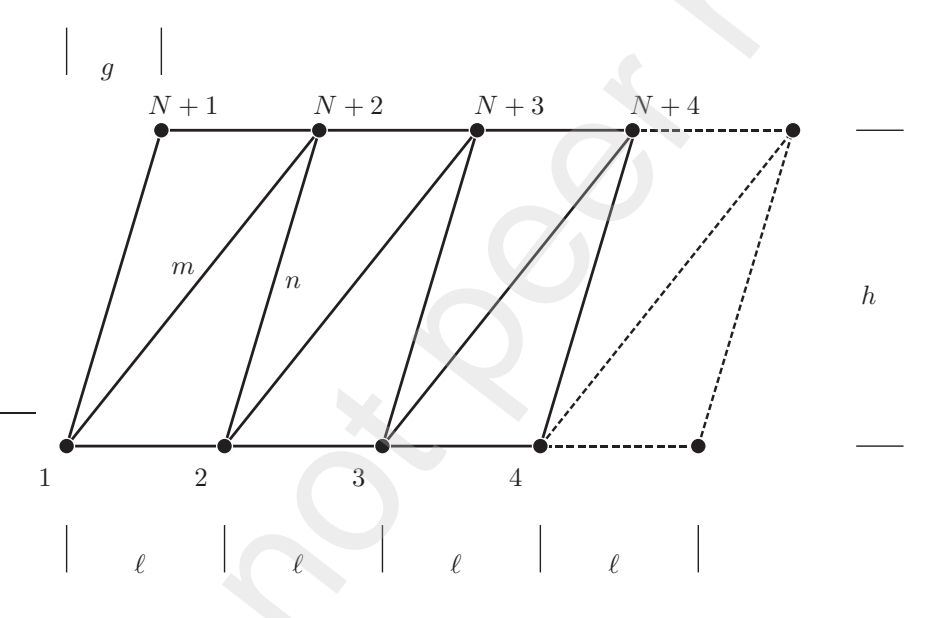


FIGURE 20. Four-stage K-tube subjected to shearing test. Polar plots of the norm of the vector collecting all the vertical displacements vs. the prescribed displacement direction angle (in degrees) at 1, 2, 3, and 4 seconds for  $a/b = \infty$ ,  $a/b = 10^5$  and  $a/b = 10^3$ .



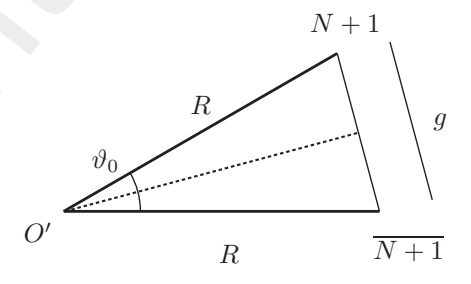


FIGURE 21. Relationship between K-tube planar folding pattern and initial configuration.